Seismic response of cylinder assemblies in axial flow

Roberto Capanna[1]†, Guillaume Ricciardi[1], Emmanuelle Sarrouy[2] and Christophe Eloy[3]

[1]CEA, DES, IRESNE, Department of Nuclear Technology, Cadarache, 13108, Saint-Paul-Lez-Durance, France

[2]Aix Marseille Univ, CNRS, Centrale Marseille, LMA UMR 7031, Marseille, France

[3]Aix Marseille Univ, CNRS, Centrale Marseille, IRPHE, Marseille, France

(Received xx; revised xx; accepted xx)

Earthquakes are a great challenge for the safety of nuclear reactors. To address this challenge, we need to better understand how the reactor core responds to seismic forcing. The reactor core is made of fuel assemblies, which are themselves composed of flexible fuel rods immersed in a strong axial flow. This gives rise to strongly-coupled fluid-structure interactions whose accurate modelling generally requires high computational costs. In this paper, we introduce a new model able to capture the mechanical response of the reactor core subjected to seismic forcing with low computational costs. This model is based on potential flow theory for the fluid part and Euler-Bernoulli beam theory for the structural part allowing us to predict the response to seismic forcing in presence of axial flow. The linear equations are solved in the Fourier space to decrease computational time. For validation purposes, we first use the proposed model to compute the response of a single cylinder in axial flow. We then implement a multiple cylinder geometry made of 4 fuel assemblies, each made of 8×8 cylinders, corresponding to an experimental facility available at CEA. The comparison between numerical results and experiments show good agreement. The model can correctly predict the added mass. It can also qualitatively capture the coupling between assemblies and the effect of confinement. This shows that a potential flow approach can give insight into the complex fluid-structure interactions within a nuclear reactor and, in particular, be used to predict the response to seismic forcing at low computational cost.

Key words:

1. Introduction

One of the main concerns for the safety of nuclear power plants is represented by earthquakes. During an earthquake, the main risk is that fuel assemblies start to move and potentially touch each other or prevent the drop of the control rods used to cool the core. To better understand the motion of fuel assemblies subjected to seismic forcing, fluid-structure interaction models are needed. In this paper, we present such a model, which has been developed with the objective of gaining insight into the complex fluid-structure interactions at play inside a nuclear reactor, while remaining computationally efficient.

† Email address for correspondence: capanna@gwu.edu

A reactor core of a pressurised water reactor (PWR) is made of fuel assemblies (between 150 and 250 depending on the power of the reactor). Each fuel assembly gathers about 100 fuel rods, stands between four and five meters high, has a cross-section of about $20 \times 20\,\mathrm{cm}^2$ and weights about 800 kg. The fuel rods, which contain the pellets of uranium, have a diameter of about 1 cm for 4 m in height; the space between each fuel rod in the assembly is about 3 mm. Fuel rods are held together by grids (between 8 and 10 depending on the power of the reactor) distributed along the height of the fuel assembly. Springs and dimples are used in-between the grid and the rods to avoid any drop of the fuel rods (De Mario & Street 1989).

The fuel assemblies are cooled down by a strong axial flow. This water flow is upwards, with velocities of about $5\,\mathrm{m\,s}^{-1}$ at 150 bar and 310 °C. The flow regime is fully turbulent with a Reynolds number based on the rod diameter of $Re \approx 5 \times 10^5$. Note that, even if the main flow is upwards, the root-mean-square-average of the transverse component is between 5 and 15% of the vertical velocity.

The presence of the water flow gives rise to strongly-coupled interactions between the fluid and the structure (Chen & Wambsganss 1972): the motion of the structure modifies the fluid flow, which itself exerts a force on the structure. A first attempt to describe fluid-structure interactions is to use the concepts of added mass and added damping. The added mass is the inertial mass added to a body because of the presence of a surrounding fluid. For simplicity it can be viewed as a volume of fluid moving with the same velocity as the body, though in reality all fluid particles will be moving to various degrees (Lamb 1895; Buat 1779). The added mass M_a of a non-deformable body moving at a velocity U through an unbounded fluid otherwise at rest can be defined such that the kinetic energy in the volume of fluid is $E_k = \frac{1}{2} M_a U^2$ or equivalently

$$M_a = \frac{\rho}{U^2} \int \|\mathbf{V}\|^2 \, dv, \tag{1.1}$$

where $\mathbf{V}$ is the velocity field. A complete collection of added mass for different geometries and flow conditions can be found in Wendel (1956) or Brennen (1982), for instance.

While the added mass is mainly due to pressure forces exerted on the body, viscous forces and boundary layer separation give rise to drag and to an added damping effect. Taylor (1952) proposed a model for the damping force on a slender structure, which has been widely used (e.g., Païdoussis 1966*a*; Triantafyllou & Cheryssostomidis 1985; Gosselin & De Langre 2011; Singh *et al.* 2012). In Taylor's model, the damping force is decomposed into two terms: a normal force akin to drag and a longitudinal force depending on the body surface and on the incident angle.

Generally, the total fluid force exerted on the non-deformable body is assumed to be decomposed into its added-mass component (proportional to the acceleration) and its drag component (proportional to the square of the velocity). This decomposition, known as the Morison equation (Morison *et al.* 1950), can correctly describe experimental observations providing drag and inertial coefficients are empirically adjusted (in general, they depend on the motion amplitude and frequency).

For deformable cylinders in axial flow, the concept of added mass does not apply directly. In that case, one can use slender body theory developed by Lighthill (1960*a*,*b*). This theory makes use of potential flow theory and arguments of momentum balance in slices of fluids along the slender body. The resulting normal force per unit length exerted by the fluid can be written in the limit of small displacement

$$F(X,T) = -M_a \left(\partial_T + U\partial_X\right)^2 W, \tag{1.2}$$

where $W(X,T)$ is the normal displacement, U is the undisturbed axial flow velocity, and

here M_a is the added mass per unit length ($M_a = \rho\pi A^2$, for a circular cylinder of radius A). In the case of a solid body, W has no X-dependence and one recovers a force opposite to $M_a\partial_T^2 W$, as expected.

Based on the work of Lighthill (1960*b*), Païdoussis (1966*a*,*b*) studied theoretically and experimentally the dynamics of a flexible slender cylinder clamped at its leading edge, which is immersed in an axial flow. He found that, above a critical flow velocity, a flutter instability appears. Later, Païdoussis (1973) and Païdoussis & Pettigrew (1979) extended this flutter stability analysis to confined geometries, by using the work of Classen (1972) and Chen & Wambsganss (1972) on added mass in confined geometries.

The stability analysis of a single cylinder in axial flow has been later generalized to clusters of cylinders (Païdoussis 1973; Païdoussis *et al.* 1977; Païdoussis & Suss 1977; Païdoussis 1979). If each cylinder is free to move independently, the fluid acts as a coupling medium and the motions of the cylinders are synchronized. Above a critical flow velocity, the coupled pinned-pinned cylinders loose stability by divergence (unstable mode of eigenfrequency zero). For higher flow velocities, the system may be subjected to several divergence and flutter instabilities simultaneously. In recent years, this work of Païdoussis has been extended (e.g., De Langre *et al.* 2007; Schouveiler & Eloy 2009; Michelin & Smith 2009) and studied numerically both for a single cylinder (De Ridder *et al.* 2013, 2015) and for a cluster of cylinders (De Ridder *et al.* 2017).

The flutter of a flexible cylinder in axial flow bears similarities with the flutter of an elastic plate often referred to as the flag instability. For a plate, two asymptotic limits can be studied: slender structures where Lighthill's slender body theory applies, and wide plates for which a two-dimensional approach is suited (Wu 2001). For intermediate aspect ratios, the pressure distribution on a flexible plate can be solved by projecting the problem in Fourier space (Guo & Païdoussis 2000; Eloy *et al.* 2007, 2008; Doaré *et al.* 2011*a*; Eloy *et al.* 2010; Doaré *et al.* 2011*b*). With this projection, the approaches of slender body approximation and large span approximation can be generalised to any aspect ratio. In this paper, we will follow a similar approach to describe the flow around assemblies of flexible cylinders found in PWR.

A different approach was proposed by Ricciardi *et al.* (2009) using a porous medium method. It becomes now possible to model both the fluid and the structure dynamics of a whole core. Some local information is lost compared to a direct numerical simulation, such as the vibrations of individual rods, but fluid-mediated interactions between fuel assemblies can be modelled. This model shows good agreement with experimental results on the response of the whole core to external forcing, but computational cost remains high.

At present, the models describing the fluid-structure interactions within a reactor core can be divided into two families: (1) complex numerical models with high computational costs, which usually hinder the understanding of physical mechanisms; and (2) linear models with low computational costs, which do not capture important mechanisms such as fluid-mediated interactions between assemblies. In this paper, we introduce a new model based on potential flow theory, with the objective of providing an accurate, computationally effective modelling of fluid-structure interactions within a reactor core.

The paper is organised as follows. In §2 the model is presented and the mathematical methodology used to solve the problem is described. The model is then applied to a single cylinder in §3 and compared to results of the literature for validation purposes. In §4, it is applied to a multiple cylinder geometry, replicating the geometry of an experimental facility. Numerical results are compared to experimental data and discussed in §5. Finally, in §6, some conclusions are drawn.

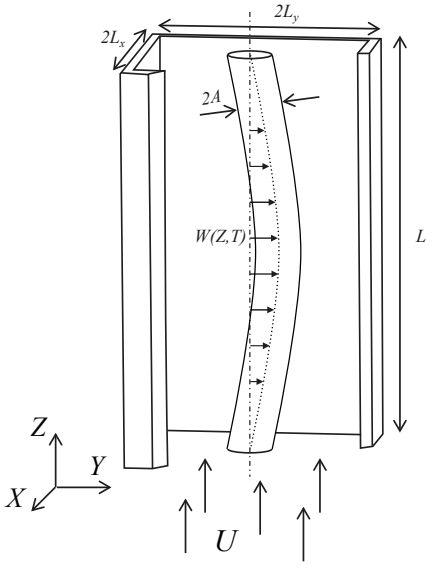

(a) Real space.

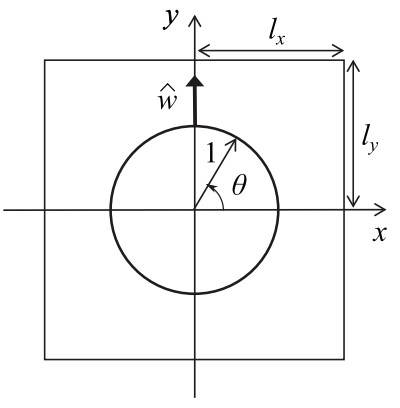

(b) Fourier space.

Figure 1: Representation of confined pinned-pinned cylinder deformed under axial flow in real space and in Fourier space.

2. Potential flow model

In this section, we describe the proposed model where the fluid flow is treated as potential and the structure as an Euler-Bernoulli beam. The model is introduced for a single cylinder in axial flow, but as we shall see, it can be generalised to multiple cylinders.

2.1. *Problem statement*

We consider a pinned-pinned cylinder of length L and radius A (Figure 1a). We will use two coordinate systems: a Cartesian system (X, Y, Z) with its origin at the bottom of the cylinder and a cylindrical system (R, θ, Z) with same origin (Figure 1a).

The cylinder is immersed in a uniform axial flow with velocity U and bounded in the X and Y directions by rigid walls at distances L_x and L_y from the cylinder axis. Without loss of generality, we consider that the cylinder deflects in the Y-direction and the deflection is called $W(Z, T)$ (Figure 1a).

We use the linearised Euler-Bernoulli beam equation (Bauchau & Craig 2009) to describe the dynamics of the cylinder deflection

$$M_s \partial_T^2 W + B \partial_Z^4 W = F_Y, \tag{2.1}$$

where M_s is the mass of the cylinder per unit length, $B = EI$ is the bending rigidity (E being Young's modulus and $I = \frac{1}{4}\pi A^4$ the second moment of area), and F_Y is the force per unit length that the fluid exerts on the cylinder in the Y-direction.

We assume that the forces exerted by the fluid on the structure are mainly originating from pressure difference. Hence, the force per unit length can be expressed as

$$F_Y(Z, T) = -\int_0^{2\pi} P(A, \theta, Z, T) \sin(\theta)\, A d\theta, \tag{2.2}$$

where $P(R, \theta, Z, T)$ is the pressure field in cylindrical coordinates.

The problem is made dimensionless using the cylinder radius A, the flow velocity U and

the fluid density ρ as characteristic length, speed and density. Dimensionless quantities are designated with lowercase letters such that, for instance

$$r = \frac{R}{A}, \quad w = \frac{W}{A}, \quad z = \frac{Z}{A}, \quad l_x = \frac{L_x}{A}, \quad l_y = \frac{L_y}{A}, \quad t = \frac{UT}{A}, \quad p = \frac{P}{\rho U^2}.$$

In dimensionless form, the linearised Euler-Bernoulli equation (2.1) becomes

$$m\,\partial_t^2 w + b\,\partial_z^4 w = f_y, \tag{2.3}$$

where

$$m = \frac{M_s}{\rho A^2}, \qquad b = \frac{B}{\rho U^2 A^4}, \qquad f_y = \frac{F_Y}{\rho U^2 A}.$$

The flow is assumed to be potential, inviscid and incompressible, such that the flow velocity is given by

$$\mathbf{V} = U\mathbf{e}_z + \nabla\Phi, \tag{2.4}$$

where $\mathbf{e}_z$ is the unit vector along z and $\Phi(X, Y, Z, T)$ is the perturbation potential. In dimensionless units, this potential is $\phi = \Phi/(UA)$. To find the flow around the moving cylinder, one has to solve a Laplace problem with Neumann boundary conditions (linearised for small displacements)

$$\Delta\phi = 0, \tag{2.5}$$

$$\left.\frac{\partial\phi}{\partial x}\right|_{|x|=l_x} = 0, \tag{2.6}$$

$$\left.\frac{\partial\phi}{\partial y}\right|_{|y|=l_y} = 0, \tag{2.7}$$

$$\left.\frac{\partial\phi}{\partial n}\right|_{r=1} = -(\partial_t + \partial_z)w(z,t)\sin\theta, \tag{2.8}$$

where (2.6) and (2.7) come from the impermeability of the walls and (2.8) from the impermeability on the cylinder wall.

Using the linearised unsteady Bernoulli equation, the dimensionless pressure field can be linked to ϕ (Capanna 2018)

$$p(x, y, z, t) = -(\partial_t + \partial_z)\phi. \tag{2.9}$$

Using this relation and applying the operator $(\partial_t + \partial_z)$ to the system (2.5–2.8) above yields

$$\Delta p = 0, \tag{2.10}$$

$$\left.\frac{\partial p}{\partial x}\right|_{|x|=l_x} = 0, \tag{2.11}$$

$$\left.\frac{\partial p}{\partial y}\right|_{|y|=l_y} = 0, \tag{2.12}$$

$$\left.\frac{\partial p}{\partial n}\right|_{r=1} = (\partial_t + \partial_z)^2 w(z,t)\sin\theta. \tag{2.13}$$

It shows that the pressure field is also a solution to a Laplace equation with Neumann boundary conditions. This is why the term P/ρ is called the acceleration potential in airfoil theory.

2.2. *Problem in Fourier space*

To solve the set of equations (2.10–2.13), we will use the method proposed by Doaré *et al.* (2011*b*). It consists in expressing the Laplace problem in Fourier space along z

$$\hat{p}(x, y, k, t) = \mathcal{F}\left[p(x, y, z, t)\right], \tag{2.14}$$

where $\hat{p}$ is the Fourier transform of p with $\mathcal{F}\left[\cdot\right]$ defined as follows

$$\mathcal{F}\left[f(z)\right] = \frac{1}{2\pi}\int_{-\infty}^{+\infty} f(z)e^{-ikz}\,dz = \hat{f}(k), \tag{2.15}$$

together with the inverse Fourier transform

$$\mathcal{F}^{-1}\left[\hat{f}(k)\right] = \int_{-\infty}^{+\infty} \hat{f}(k)e^{ikz}\,dk = f(z). \tag{2.16}$$

The convolution product along z, noted $\star$, is also introduced

$$f \star g = \int_{-\infty}^{+\infty} f(\zeta)g(z-\zeta)\,d\zeta = 2\pi\mathcal{F}^{-1}\left[\hat{f}\,\hat{g}\right]. \tag{2.17}$$

In Fourier space, the three-dimensional Laplace problem is transformed into a two-dimensional Helmholtz problem

$$(\partial_x^2 + \partial_y^2)\hat{p} = k^2\hat{p}, \tag{2.18}$$

$$\left.\frac{\partial\hat{p}}{\partial x}\right|_{|x|=l_x} = 0, \tag{2.19}$$

$$\left.\frac{\partial\hat{p}}{\partial y}\right|_{|y|=l_y} = 0, \tag{2.20}$$

$$\left.\frac{\partial\hat{p}}{\partial n}\right|_{r=1} = \hat{\gamma}(k,t)\sin\theta, \tag{2.21}$$

where $\hat{\gamma}(k,t)$ is the Fourier transform of the impermeability boundary condition, such that

$$\hat{\gamma} = \mathcal{F}\left[(\partial_t + \partial_z)^2 w\right]. \tag{2.22}$$

Equation (2.2) relates the force per unit length exerted by the fluid on the cylinder and the pressure field. Using dimensionless quantities and taking the Fourier transform of (2.2), one obtains the equivalent in Fourier space

$$\hat{f}_y(k,t) = -\int_0^{2\pi} \hat{p}(r=1,\theta,k,t)\sin\theta\,d\theta, \tag{2.23}$$

where $\hat{f}_y$ is the Fourier transform of f_y. The pressure $\hat{p}$ being solution of the linear Helmholtz problem (2.18–2.21), its solution is proportional to $\hat{\gamma}(k,t)$. Hence, (2.23) can be written

$$\hat{f}_y = -\hat{\mu}(k)\hat{\gamma}(k,t). \tag{2.24}$$

where the function $\hat{\mu}(k)$ depends on l_x and l_y through the boundary conditions (2.19) and (2.20).

Equation (2.3) governing beam dynamics then becomes in Fourier space

$$m\partial_t^2\hat{w} + k^4 b\hat{w} = \hat{\mu}(k)\left[-(\partial_t^2\hat{w} + 2ik\partial_t\hat{w} - k^2\hat{w})\right], \tag{2.25}$$

showing that $\hat{\mu}$ plays the role of an added mass in Fourier space and that added damping $2ik\hat{\mu}$ and added stiffness $-k^2\hat{\mu}$ are proportional to this added mass.

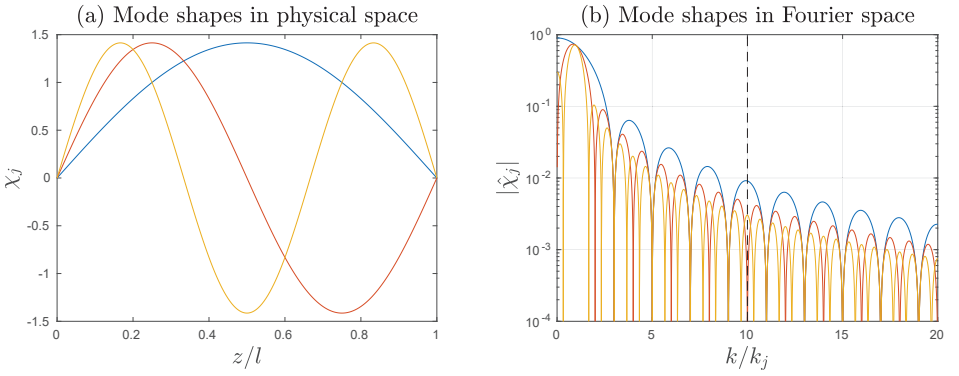

Figure 2: (a) Eigenmodes for the first 3 modes of a pinned-pinned beam and (b) their Fourier transform.

The objective now will be to calculate the added mass $\hat{\mu}(k)$. In practice, to calculate it, we can assume $\hat{\gamma} = 1$, compute numerically the solution $\hat{p}$ of the Helmholtz problem (2.18–2.21) for different values of k, l_x and l_y, and finally use (2.23) and (2.24) to compute $\hat{\mu}(k)$.

2.3. *Modal decomposition and range of interest for k*

Considering an external forcing at a given frequency Ω, the displacement of the cylinder can be written in dimensionless form as

$$w(z,t) = \sum_{j=1}^{\infty} q_j(t)\chi_j(z), \tag{2.26}$$

where $\chi_j(z)$ are the beam eigenmodes and $q_j(t) = \eta_j e^{i\omega t}$ the generalised coordinates, with η_j the modal amplitudes (which do not depend on time), and $\omega = \Omega A/U$ the dimensionless forcing frequency.

To determine the interesting range for k for which $\hat{\mu}$ should be computed, let us examine the eigenmodes $\chi_j(z)$ and their Fourier transform $\hat{\chi}_j(k)$ for pinned-pinned beams. Eigenmodes are given by Blevins (2015)

$$\chi_j(z) = \sqrt{2}\sin(k_j z), \quad \text{with } k_j = j\pi/l, \tag{2.27}$$

with $l = L/A$ the dimensionless cylinder length. Using this normalisation, the scalar product of two eigenmodes is

$$\langle \chi_i, \chi_j \rangle = \frac{1}{l}\int_0^l \chi_i(z)\chi_j(z)\,dz = \delta_{ij}. \tag{2.28}$$

As Figure 2(b) shows, k values greater than $10k_j$ have contributions at least 100 times smaller than low k values in Fourier space. Hence, they can be truncated.

Classical values for PWR beams are $A \in [10^{-3}, 10^{-2}]\,\mathrm{m}$ and $L \in [1, 10]\,\mathrm{m}$. Hence, classical slenderness ratios l belong to $[10^2, 10^4]$ and dimensionless wavenumbers $k_j = j\pi/l \in [3{\times}10^{-4}, 0.3]$ when considering the first 10 modes. This implies that the interesting range for which $\hat{\mu}$ should be evaluated is roughly $k \in [10^{-4}, 10]$.

2.4. *Equation of motion in generalised coordinates*

Taking the Fourier transform of the modal decomposition (2.26), inserting it into the beam equation (2.25) in Fourier space, performing an inverse Fourier transform,

and taking the scalar product (2.28) with the eigenmodes χ_j gives a set of differential equations for the generalised coordinates $q_i(t)$ that can be written in vector form as

$$\boldsymbol{M}\,\ddot{\mathbf{q}} + \boldsymbol{K}\,\mathbf{q} = -\left(\boldsymbol{M_a}\,\ddot{\mathbf{q}} + \boldsymbol{C_a}\,\dot{\mathbf{q}} + \boldsymbol{K_a}\,\mathbf{q}\right), \tag{2.29}$$

where $\mathbf{q}(t) = [q_1(t), q_2(t), \cdots]^T$ is the vector of generalised coordinates, the left-hand side corresponds to the unforced beam equation, and the right-hand side corresponds to the forcing by pressure forces. Here, we have omitted the external forcing term representing the seismic forcing.

The matrix $\boldsymbol{M} = m\boldsymbol{I}$, with $\boldsymbol{I}$ the identity matrix, is the mass matrix, and $\boldsymbol{K} = b\,\boldsymbol{diag}(\{k_j^4\})$ is the stiffness matrix (where $\boldsymbol{diag}(\{k_j^4\})$ means the diagonal matrix with k_1^4, k_2^4, etc. on the diagonal). Equating the left-hand side of (2.29) to zero allows to recover the eigenmodes and the eigenfrequencies $\omega_j = \sqrt{bk_j^4/m}$ of the beam in vacuum.

The matrices $\boldsymbol{M_a}$, $\boldsymbol{C_a}$, and $\boldsymbol{K_a}$ correspond to the added mass, added damping and added stiffness matrices respectively. Their coefficients can be calculated as

$$(\boldsymbol{M_a})_{ij} = \langle \chi_i, \mathcal{F}^{-1}\left[\hat{\mu}\hat{\chi}_j\right]\rangle = \frac{1}{2\pi}\langle \chi_i, \mu \star \chi_j\rangle, \tag{2.30a}$$

$$(\boldsymbol{C_a})_{ij} = \langle \chi_i, \mathcal{F}^{-1}\left[2ik\hat{\mu}\hat{\chi}_j\right]\rangle = \frac{1}{2\pi}\langle \chi_i, 2\mu \star \chi_j'\rangle, \tag{2.30b}$$

$$(\boldsymbol{K_a})_{ij} = \langle \chi_i, \mathcal{F}^{-1}\left[-k^2\hat{\mu}\hat{\chi}_j\right]\rangle = \frac{1}{2\pi}\langle \chi_i, \mu \star \chi_j''\rangle, \tag{2.30c}$$

where χ_j' and χ_j'' respectively denote first and second derivatives of χ_j, $\mu = \mathcal{F}^{-1}\left[\hat{\mu}\right]$ and we have used the property (2.17) of the convolution product.

We see here that the knowledge of $\hat{\mu}(k)$ or $\mu(z)$ is enough to compute the matrices $\boldsymbol{M_a}$, $\boldsymbol{C_a}$, and $\boldsymbol{K_a}$. In addition, these matrices only depend on the geometry of the problem (i.e. the wall distances l_x and l_y) and not on the forcing. Finally, note that the Helmholtz problem (2.18) only depends on k^2, which means that $\hat{\mu}(k)$ and $\mu(z)$ are real and even functions. The coefficients of the matrices $\boldsymbol{M_a}$, $\boldsymbol{C_a}$, and $\boldsymbol{K_a}$ are thus all real, as expected.

3. Single cylinder

In this section, the numerical calculations performed for the single cylinder geometry using the code implemented on FreeFEM++ (Hecht 2012*a*,*b*) will be presented. FreeFEM++ requires the weak formulation of problems. Problem (2.18)-(2.21) is then implemented as follows

$$\int_{\partial\mathcal{C}} v\,\sin(\theta)\,dS - \int_{\mathcal{D}} (\nabla\hat{p}\cdot\nabla v + k^2\hat{p}v)\,dV = 0, \forall v$$

where $\partial\mathcal{C}$ denotes the rod's boundaries and $\mathcal{D}$ the fluid domain (see Appendix A).

3.1. *Meshing*

As previously described, the numerical resolution of the problem takes advantage of the Fourier transform. This allows us to solve several 2D problems, instead of solving a 3D problem.

In this section, we present numerical solutions of the Helmholtz problem described by (2.18–2.21). Our objective is to compute the value of the function $\hat{\mu}(k; l_x, l_y)$ for different values of k, l_x and l_y. Thanks to the symmetries of the problem, the equations can be solved on a quarter of the domain only (Figure 3).

Before showing the results of these numerical computations, some considerations have

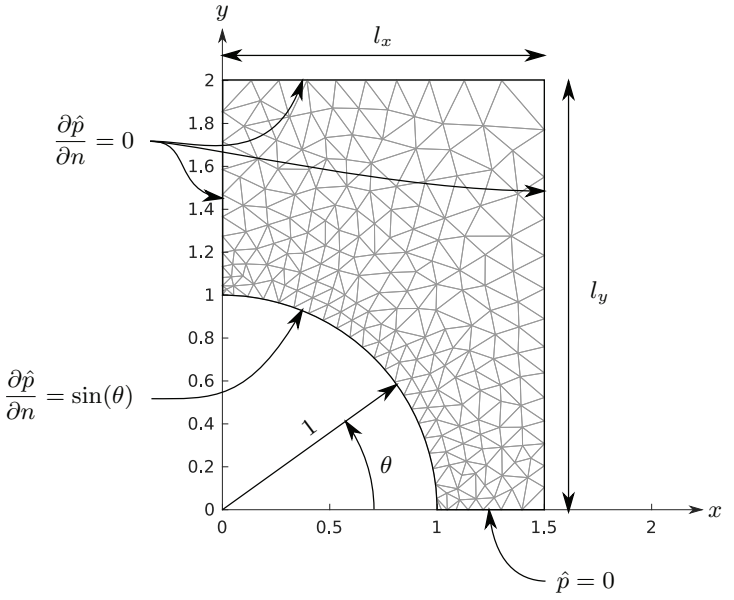

Figure 3: Helmholtz problem represented in the FEM domain: limit conditions and example mesh for $k = 0.01$, $l_x = 1.5$ and $l_y = 2$.

to be made on the discretisation of the domain. A convergence study has been performed in order to find the optimal meshing for different combinations of wall distance and wave number. Typically, the size of the meshes must be decreased when the wave number k is increased. In addition, the refinement of meshes will increase as the enclosure size decreases and when getting closer to the cylinder.

Explored values are $k \in [10^{-5}, 10^{3}]$, $l_x, l_y \in [1.25, 50]$. The variations of the number of cells in the mesh with l_x and l_y do not depend on k: number of cells is maximum for $l_x = l_y = 5$. This maximum is equal to 864 for $k \leqslant 1$ and increases quadratically for $k > 1$. The FreeFEM++ code used in this study is included in Appendix A. Raw data can be found in the csv file attached to this article; it contains the 2448 combinations of l_x, l_y and k values and the resulting $\hat{\mu}$ values.

3.2. *General trends*

Figure 4 shows the dependence of the added mass $\hat{\mu}$ on the wavenumber k for different values of the wall distances l_x and l_y. It shows the added mass does not change substantially for $k \lesssim 10^{-2}$ or $k \gtrsim 10^{2}$, for the enclosure sizes considered. This was expected because the only scales in the problem are the radius $a = 1$ and the enclosure lengths l_x and l_y, which are of order 1. Hence, for l_x and l_y fixed, most variations of the added mass are expected to occur near $k \approx 1$. Note that the slenderness ratio of cylinders in a reactor core assembly is very large and the range of relevant wavenumbers in this context is $k \in [3 \times 10^{-4}, 0.3]$, as stressed already in §2.3. For the sake of clarity, the raw data used for the plots in Figure 4 are published online joint to this paper.

3.3. *Slender body limit*

In the asymptotic limit of large wavelengths ($k \ll 1$) and large enclosure sizes ($l_x, l_y \gg 1$), we expect to recover the result of slender body theory Lighthill (1960*b*) given by (1.2),

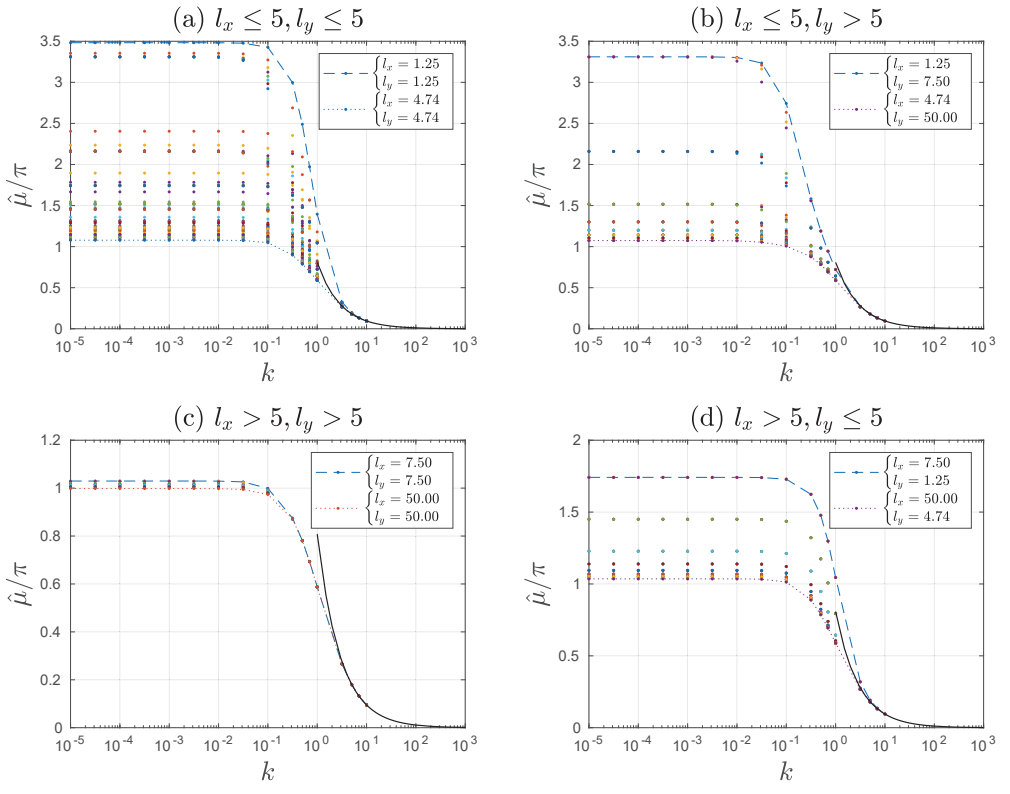

Figure 4: Value of $\hat{\mu}$ as function of the wavenumber k for different values of the wall distances l_x and l_y. Dots denote computed values and the solid line shows the fit (3.5), valid for $k \geqslant 10$.

which writes in dimensionless form

$$f_y = -m_a(\partial_t + \partial_z)^2 w, \tag{3.1}$$

with $m_a = \pi$, the added mass per unit length of a circular cylinder in dimensionless units. By analogy with (2.24), one thus expects

$$\lim_{k\to 0} \hat{\mu} = \pi, \quad \text{for } l_x, l_y \gg 1, \tag{3.2}$$

and this is indeed what is found numerically when $l_x \gtrsim 10$, $l_x \gtrsim 10$, and $k \lesssim 10^{-2}$ (Figure 4c). This validates our numerical results for small wavenumbers k, in the limit of negligible enclosure sizes.

3.4. *Comparison with cylinder in annular enclosure*

In the previous section, the numerical computations of the added mass have been validated in the limit of long wavelengths and large enclosure size by comparison with the slender body theory of Lighthill (1960*b*). In this section, we perform further comparisons with the theoretical results of Chen (1985) on a single cylinder confined in a concentric annular chamber. In a potential flow, the added mass of such a cylinder is

$$\hat{\mu} = \pi \frac{a_{\text{ext}}^2 + 1}{a_{\text{ext}}^2 - 1}, \tag{3.3}$$

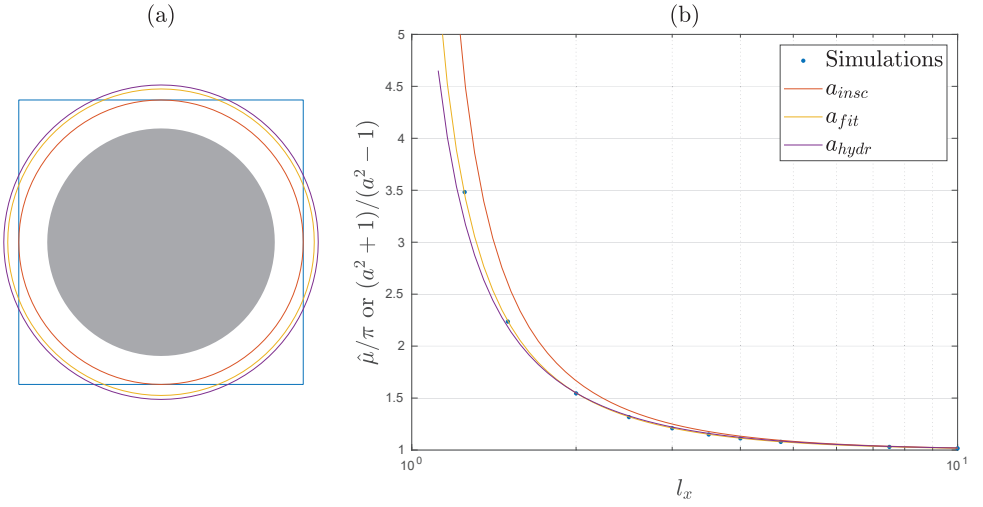

Figure 5: Comparison between the computed added mass of a single cylinder in squared enclosure and the theoretical predictions of Chen (1985) for a concentric annular enclosure. (a) Geometry of the squared enclosure ($l_x = l_y = 1.25$) superimposed with the three proposed annular enclosure radii: a_{hydr}, a_{insc}, and a_{fit}. (b) Comparison between our numerical results (dots) for $l_x = l_y$ and the prediction given by (3.3) for the three proposed radii (solid lines).

where a_{ext} is the radius of the annular enclosure in dimensionless units.

We will compare this prediction with our numerical calculations of a cylinder in a squared enclosure ($l_x = l_y$). To perform this comparison, we need to relate the wall distances $l_x = l_y$ to the annular radius a_{ext}. One possibility is to use the hydraulic diameter equivalence, which leads to an annular radius

$$a_{\text{hydr}} = 1 + \frac{4{l_x}^2 - \pi}{4l_x + \pi}. \tag{3.4}$$

Alternatively, one can simply use the inscribed circle, which gives an annular radius $a_{\text{insc}} = l_x$. Finally, one can look for the best linear fit with the numerical data, which leads to $a_{\text{fit}} = 1.0775\, l_x$.

Figure 5 shows a comparison between our computations of the added mass for a squared enclosure ($l_x = l_y$ and $k \ll 1$) and the added mass predicted by (3.3) for an annular enclosure. This comparison shows that the effect of the squared enclosure is equivalent to an annular enclosure with radius $a_{\text{fit}} = 1.0775\, l_x$. The hydraulic diameter equivalence gives a good estimate of the effect of the enclosure. This validates our numerical calculations in a squared enclosure geometry in the limit $k \ll 1$.

3.5. *Confinement effects*

Figure 4 shows that $\hat{\mu}$ does change significantly for small values of k, but still depends on the wall distances l_x and l_y when $l_x \lesssim 5$ or $l_y \lesssim 5$. Two extreme cases can be considered: (1) a small value of the wavenumber $k = 10^{-5}$; and (2) a large value $k = 10$.

Figure 6 shows how the added mass depends on both l_x and l_y for the two extreme wavenumbers considered ($k = 10^{-5}$ and $k = 10$). For $k = 10^{-5}$, the enclosure length along the x-direction has much more influence than its counterpart along the y-direction (Figure 6a). For $k = 10$, it is the opposite. Note however that these effects have different

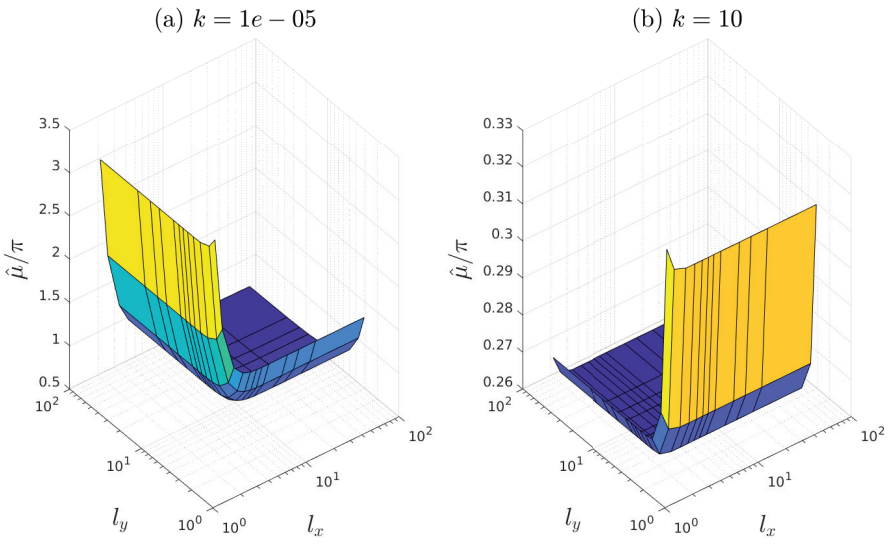

Figure 6: Confinement effects for (a) small wavenumbers and (b) big wavenumbers.

magnitudes: for $k = 10^{-5}$, the value of $\hat{\mu}$ roughly triples between $l_x = 10$ and $l_x = 1.25$, while, for $k = 10$, $\hat{\mu}$ varies only by 15% between $l_y = 10$ and $l_y = 1.25$.

Figure 4 thus shows that, for large wavenumbers, the dependency on the enclosure size is weak. Assume that $\hat{\mu}$ is independent of l_x and l_y for large k values, we can find a power-law approximation of $\hat{\mu}$ displayed as black solid line in Figure 4

$$\hat{\mu} \approx 2.5\, k^{-1}, \;\; k \geqslant 10. \tag{3.5}$$

For small wavenumbers, although the cylinder can only move in the y direction, it is the wall distance along x that has the strongest influence. To better understand this paradoxical result, we plot the velocity field in the Fourier space (Figure 7). For $k = 10^{-5}$, a strong flow in the y direction (opposite to the cylinder displacement) is observed along the wall $x = l_x$ around the cylinder diameter ($y \approx 0$) as shown in Figure 7a. For large wavenumbers however, no such flow is observed (Figure 7b). By virtue of mass conservation, when the wall distance along x is reduced, this flow increases. This is why there is a strong dependency of the fluid-structure interaction force on the x direction confinements for small wavenumbers.

Finally, for all the wavenumbers that have been considered and for all enclosure sizes, the added mass $\hat{\mu}$ appears to increase as the enclosure lengths decrease (in both directions). This observation is in agreement with the literature on channel flows made by Chen & Wambsganss (1972); Chen (1985); Païdoussis & Pettigrew (1979).

The calculations performed for a single cylinder geometry allowed us to prove the reliability of the proposed simplified model. The introduction of the potential flow theory and the use of Fourier transform are key to directly relate the cylinder displacement and the resulting pressure force.

This approach leads to fast calculations for any kind of geometry. In the next section, it will be applied to a group of cylinders and compared to experimental results in the same geometry.

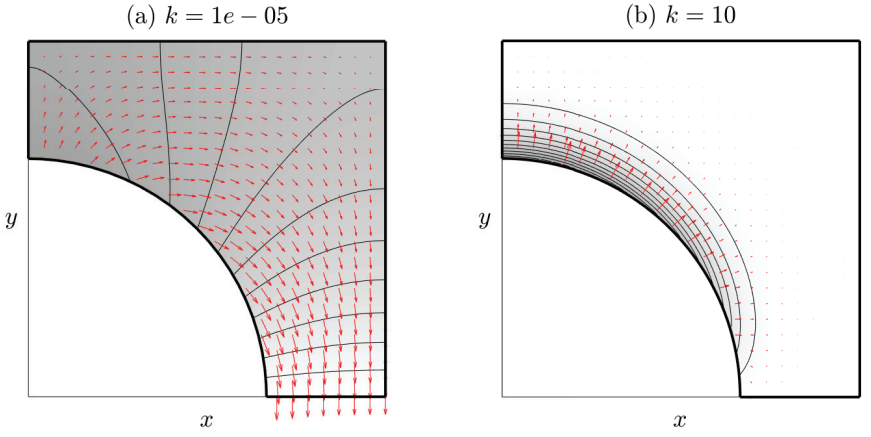

Figure 7: Velocity and pressure fields in Fourier space for both small and large wavenumbers.

4. Assemblies of cylinders

This section is dedicated to a geometry with multiple cylinders. This geometry is built to represent the four surrogate fuel bundles of the experimental facility ICARE that we used to validate our results.

4.1. *ICARE experimental apparatus*

The ICARE experimental facility is made of a closed water loop powered by a centrifugal pump, the test-section, a compensation tank and a heat exchanger (Figure 8). The test-section is placed in vertical position with a square section of 22.5 cm x 22.5 cm and hosts up to 4 fuel assemblies arranged in a 2 x 2 lattice. The length of the fuel assemblies is $L = 2.57$ m. Each of them is constituted of a squared lattice of 8×8 rods, in which there are 60 rods simulating fuel rods made of acrylic and 4 stainless steel guide tubes. The guide tubes are empty inside, and they are welded to 5 metallic spacer grids along the length of the assembly. The guide tubes have a structural function since they give rigidity to the assembly and they hold together fuel rods. Each assembly has a section of $10.1 \times 10.1\,\mathrm{cm}^2$, and the 60 rods constituting it have a diameter of $2A = 9$ mm with a pin pitch $P/(2A) = 1.39$. The top and bottom of the assembly are rigidly fixed to the guide tubes, and they are fixed to the test-section through the lower support plate and the upper support plate.

A hydraulic actuator applies dynamic forcing to one of the four fuel assemblies (assembly 1 in Figure 8). This forcing in one dimension aims to simulate an earthquake. The actuator is screwed into one of the grids of the assembly and a force sensor is installed in-between the actuator and the stem.

The test-section is equipped with 24 linear variable differential transformer (LVDT) position sensors to measure the displacement of each grid in two directions (Figure 9). For more details on the ICARE experiment, please refer to Capanna *et al.* (2019).

4.2. *Problem geometry and meshing*

The ICARE geometry is implemented in the code to allow for comparison with experiments with large ($C = 8$ mm) or small ($C = 4$ mm) confinements (Figures 10a and 10b respectively). Confinement size denotes the length of the gap between different

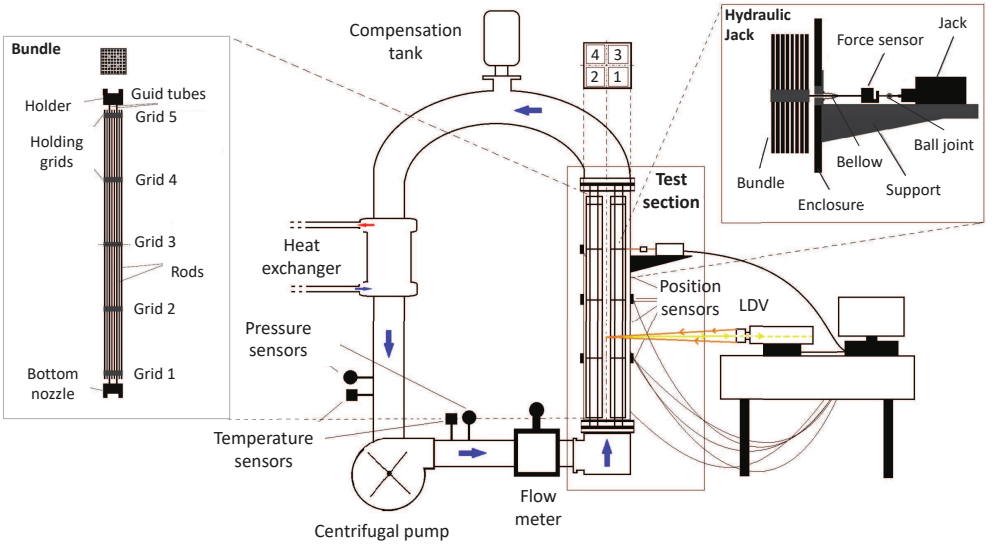

Figure 8: Scheme of the ICARE experimental facility.

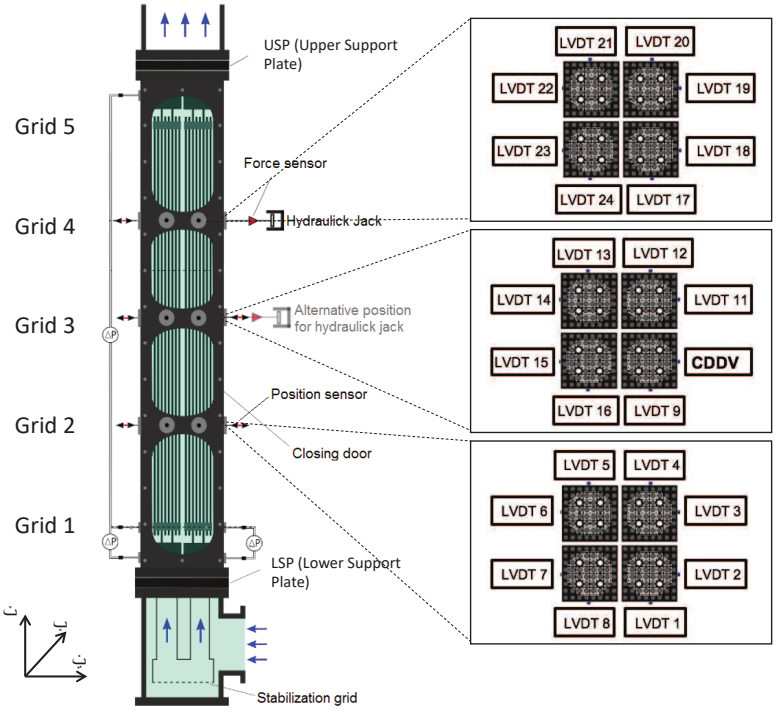

Figure 9: Scheme of the displacement sensors on the ICARE test-section.

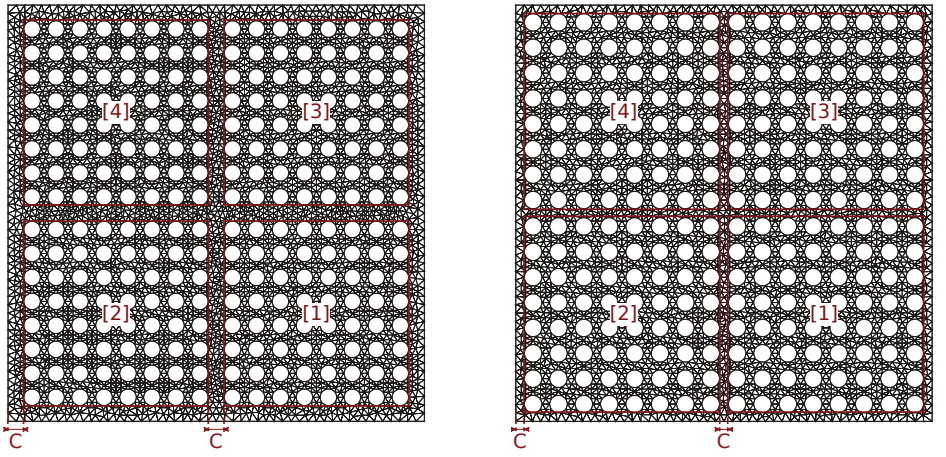

(a) 4 assemblies in large confinement. (b) 4 assemblies in small confinement.

Figure 10: Mesh for the two configurations simulating the ICARE set-up. These two geometries only differ by the value of the confinement C as pictured.

assemblies and between the assemblies and the walls. For both confinement sizes the distance in-between the rods of the same assembly remains the same.

Assemblies are numbered as depicted in Figure 10a. As in the experiments, the rods of assembly [1] are forced along the x-direction and they all exhibit the same displacement $w_x^{[1]}(z,t)$. Those rods are assumed not to move along y direction and the rods in the other assemblies are assumed not to move.

Based on §3, the Helmholtz problem to solve is

$$\Delta\hat{p} = k^2\hat{p}, \qquad \text{in the domain,} \tag{4.1a}$$

$$\left.\frac{\partial\hat{p}}{\partial n}\right|_{\partial\text{Cas.}} = 0, \qquad \text{on the walls,} \tag{4.1b}$$

$$\left.\frac{\partial\hat{p}}{\partial n}\right|_{\partial\mathcal{C}^{[1]}} = \hat{\gamma}_x^{[1]}(k,t)\cos(\theta), \qquad \text{for assembly [1],} \tag{4.1c}$$

$$\left.\frac{\partial\hat{p}}{\partial n}\right|_{\partial\mathcal{C}^{[n]}} = 0, \qquad \text{for other assemblies,} \tag{4.1d}$$

where the superscripts $[n]$ refer to the assembly number, $\partial\mathcal{C}^{[n]}$ denotes the boundaries of rods of assembly $[n]$ (with θ the local polar angle for each rod) and

$$\hat{\gamma}_x^{[1]} = \mathcal{F}\left[(\partial_t + \partial_z)^2 w_x^{[1]}\right]. \tag{4.2}$$

As in §3, the solution $\hat{p}$ of the Helmholtz problem (4.1) is proportional to $\hat{\gamma}_x^{[1]}$ and one can define added masses $\hat{\mu}_x^{[n]}$ and $\hat{\mu}_y^{[n]}$ from the forces exerted on each assembly

$$\hat{f}_x^{[n]}(k,t) = -\int_{\partial\mathcal{C}^{[n]}} \hat{p}\cos(\theta)\,d\theta = -\hat{\mu}_x^{[n]}\hat{\gamma}_x^{[1]}, \tag{4.3a}$$

$$\hat{f}_y^{[n]}(k,t) = -\int_{\partial\mathcal{C}^{[n]}} \hat{p}\sin(\theta)\,d\theta = -\hat{\mu}_y^{[n]}\hat{\gamma}_x^{[1]}. \tag{4.3b}$$

In practice, $\hat{\mu}_x^{[n]}$ and $\hat{\mu}_y^{[n]}$ can be calculated by assuming $\hat{\gamma}_x^{[1]} = 1$ and numerically solving the Helmholtz problem (4.1) for $\hat{p}$. The convergence of the calculations depends

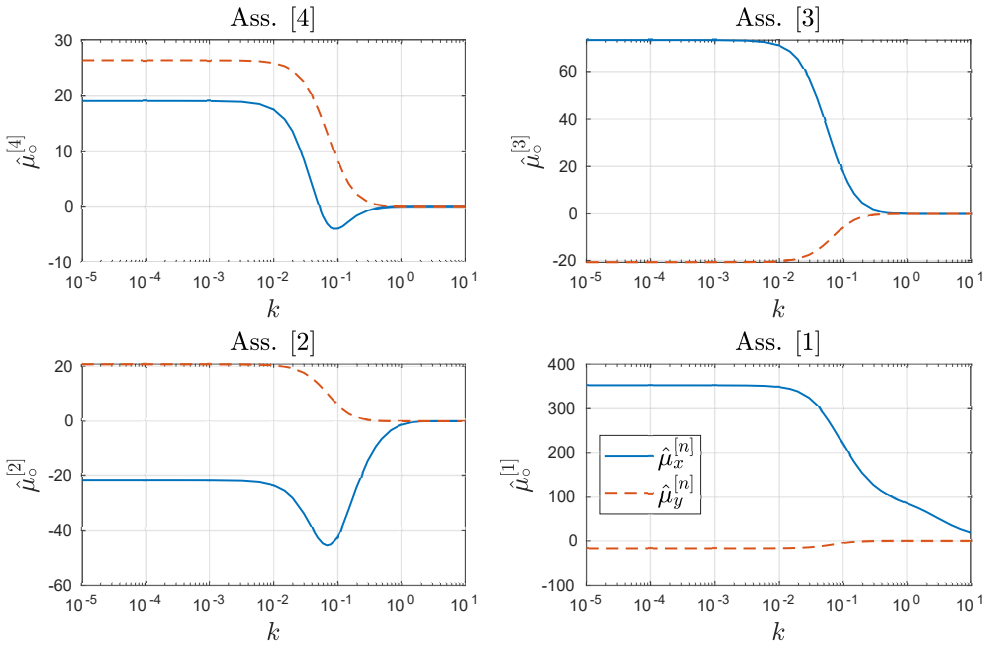

Figure 11: Added masses $\hat{\mu}_x^{[n]}$ (blue solid line) and $\hat{\mu}_y^{[n]}$ (red dashed line) on each assembly (in Fourier space) for different values of k.

on the mesh size. We thus conducted a convergence study and found that convergence is ensured when the walls are divided at least into 150 sections, and the cylinder borders into 50 sections. The calculations presented here have been performed with 200 divisions on the external walls and 75 divisions on the cylinder borders, which corresponds to approximately 500 000 cells in the domain and a computing time of about 60 s.

Figure 11 shows the results of these computations for $k \in [10^{-5}, 10]$. In Appendix B, we detail these results for individual rods. As in the single-cylinder case, the added masses do not change much for extreme values of k, i.e. $k \lesssim 10^{-2}$ or $k \gtrsim 1$, except for assembly [1], the forced assembly. For large k, the added masses converge to zero.

4.3. *Equations of motion in real space*

The functions $\hat{\mu}_x^{[n]}(k)$ and $\hat{\mu}_y^{[n]}(k)$ can be interpolated using piecewise 6th-order polynomials, which can then be used to calculate $\mu_x^{[n]}(z)$ and $\mu_y^{[n]}(z)$ with an inverse Fourier transform (appendix C). By analogy with the calculations for a single cylinder done in §2.4, we can define added mass, added damping, and added stiffness matrices for the assemblies too. There are 24 such matrices: 3 kinds (mass $\boldsymbol{M}$, damping $\boldsymbol{C}$, stiffness $\boldsymbol{K}$), 2 axes (x and y, subscript $\circ$) and 4 assemblies noted with the superscript $[n]$. Similarly to (2.30a–c), these matrices are expressed from the added masses $\mu_\circ^{[n]}(z)$

$$\left(\boldsymbol{M}_\circ^{[n]}\right)_{ij} = \langle \chi_i, \mathcal{F}^{-1}\left[\hat{\mu}_\circ^{[n]}\hat{\chi}_j\right]\rangle = \frac{1}{2\pi}\langle \chi_i, \mu_\circ^{[n]} \star \chi_j\rangle, \tag{4.4a}$$

$$\left(\boldsymbol{C}_\circ^{[n]}\right)_{ij} = \langle \chi_i, \mathcal{F}^{-1}\left[2ik\hat{\mu}_\circ^{[n]}\hat{\chi}_j\right]\rangle = \frac{1}{2\pi}\langle \chi_i, 2\mu_\circ^{[n]} \star \chi_j'\rangle, \tag{4.4b}$$

$$\left(\boldsymbol{K}_\circ^{[n]}\right)_{ij} = \langle \chi_i, \mathcal{F}^{-1}\left[-k^2\hat{\mu}_\circ^{[n]}\hat{\chi}_j\right]\rangle = \frac{1}{2\pi}\langle \chi_i, \mu_\circ^{[n]} \star \chi_j''\rangle, \tag{4.4c}$$

where $\chi_i(z)$ is the i-th beam eigenmode defined in (2.27).

Because it is forced at mid-height, we can assume that assembly [1] moves mainly in its first beam eigenmode, i.e. $w_x^{[1]}(z,t) = q_x^{[1]}(t)\chi_1(z)$. We can further assume that the added mass and added stiffness matrices are diagonal and that the added damping is negligible (appendix C). With these hypotheses, the equation of motion for the x-component of assembly [1] is

$$\left(m_s + m_x^{[1]}\right)\ddot{q}_x^{[1]} + c_v\dot{q}_x^{[1]} + \left(k_s + k_x^{[1]}\right)q_x^{[1]} = f_e e^{i\omega t}, \tag{4.5}$$

where $m_s = 64m$ is the dimensionless mass of one assembly per unit length, $k_s = 64bk_1^4$ its stiffness, c_v accounts for the damping induced by the viscosity effect, $m_x^{[1]}$ and $k_x^{[1]}$ denote the component $(1,1)$ of the added matrices $\boldsymbol{M}_x^{[1]}$ and $\boldsymbol{K}_x^{[1]}$ and $f_e e^{i\omega t}$ is the external forcing projected onto the first eigenmode with f_e a scalar. The $m_x^{[1]}$ and $k_x^{[1]}$ coefficients represent the added mass and stiffness encountered by an assembly which moves in its first mode in either x or y direction. Here, we consider only a weak coupling between the assemblies, such that we can neglect the hydrodynamic forces due to the motion of the other assemblies on assembly [1] (the validity of this assumption will be assessed below). The solution of (4.5) is simply

$$q_x^{[1]} = h_x^{[1]} f_e e^{i\omega t}, \tag{4.6}$$

with the transfer function

$$h_x^{[1]}(\omega) = \frac{1}{-\omega^2\left(m_s + m_x^{[1]}\right) + i\omega c_v + k_s + k_x^{[1]}}. \tag{4.7}$$

It is possible to estimate the motion of assemblies [2] to [4] by considering the superimposition of the two following cases: still rods undergoing fluid forces induced by assembly [1] on the one hand, and moving rods undergoing fluid forces generated by their own movement while other assemblies stand still

$$\left(m_s + m_x^{[1]}\right)\ddot{q}_\circ^{[n]} + c_v\dot{q}_\circ^{[n]} + \left(k_s + k_x^{[1]}\right)q_\circ^{[n]} = -\left(-\omega^2 m_\circ^{[n]} + k_\circ^{[n]}\right)q_x^{[1]}, \tag{4.8}$$

where the coefficients $m_x^{[1]}$, c_v, and $k_x^{[1]}$ appear on the left-hand side because, by symmetry, they also correspond to the pressure force induced by the motion $q_\circ^{[n]}$ on the assembly $[n]$ itself. The right-hand side represents the action of assembly [1] motion via the fluid.

From (4.4c), we see that the added stiffness is $k_\circ^{[n]} = -k_1^2 m_\circ^{[n]}$, with $k_1 = \pi/l$ (since $\chi_i'' = -k_i^2\chi_i$). We will now assume that $\omega \gg k_1$, which is true here because typical values of ω are around 0.3 and $l \approx 571$. This means that the added stiffness term $k_\circ^{[n]}$ can be neglected compared to the added mass term $-\omega^2 m_\circ^{[n]}$ in (4.5) and (4.8). The values of the added masses $m_\circ^{[n]}$ are given in table 1. From this table, we see that the ratio of added masses, $m_\circ^{[n]}/m_x^{[1]}$ is at most 21% (for $n > 1$). This justifies to neglect the hydrodynamic forces due to the motion of the assemblies $[n]$ onto assembly [1], which can be estimated as the square of this ratio and is thus of order 4% at most.

Under these hypotheses, we can calculate the displacement ratio at the forcing frequency ω

$$\frac{q_\circ^{[n]}}{q_x^{[1]}} \approx -\frac{-\omega^2 m_\circ^{[n]}}{-\omega^2\left(m_s + m_x^{[1]}\right) + i\omega c_v + k_s}, \tag{4.9}$$

Table 1: Added mass matrix coefficients for small and large confinement

confinement	$m_x^{[1]}$	$m_x^{[2]}$	$m_x^{[3]}$	$m_x^{[4]}$	$m_y^{[1]}$	$m_y^{[2]}$	$m_y^{[3]}$	$m_y^{[4]}$
large	350	-22.1	72.7	18.6	-17.0	20.5	-20.5	26.2
small	384	-24.0	79.0	21.3	-22.4	25.3	-25.3	29.3

which becomes at the resonant frequency ω_{res}

$$\frac{q_\circ^{[n]}}{q_x^{[1]}} \approx -i\omega_{\text{res}} \frac{m_\circ^{[n]}}{c_v}, \quad \text{with } -\omega_{\text{res}}^2 \left(m_s + m_x^{[1]} \right) + k_s = 0. \tag{4.10}$$

Note that this equation is only applicable to $n \neq 1$.

4.4. *Comparison with a periodic assembly of cylinders*

The model presented above allows us to compute the added mass of an assembly of cylinders organized in a square array. A qualitative comparison can be made with an infinite assembly made of a periodic arrangement of cylinders (Pettigrew & Taylor 2003). In this case, by analogy with (3.3), the added mass of each cylinder is expressed as

$$\hat{\mu} = \pi \frac{a_{\text{equiv}}^2 + 1}{a_{\text{equiv}}^2 - 1}, \tag{4.11}$$

where a_{equiv} is a measure of the equivalent confinement that can be approximated as

$$a_{\text{equiv}} = (0.535 + 0.14p)\, p, \tag{4.12}$$

with $p = P/A$, the period along x and y of the arrangement.

Using the value $P/A = 2.78$ of the ICARE assemblies, (4.11) corresponds to an added mass per cylinder $\hat{\mu} = 4.26$. Considering an assembly made of 64 cylinders, the total added mass is $m_x = 274$. This value can be compared to the value $m_x^{[1]} = 350$ obtained in our simulations (Table 1). The two values are of the same order, but in the ICARE geometry, the presence of other assemblies and of the walls tends to increase the added mass.

5. Comparison with experimental results

This section compares results obtained using the simplified model and results from a set of experiments conducted on the ICARE facility described in §4.1. Experiments are performed imposing a sine sweep ranging from 0 to 10 Hz with a constant amplitude of 1 mm and an axial fluid velocity of 1 m/s when water is present. To catch the transfer function of a system using a swept sinusoidal excitation, the sweep rate needs to be small enough to avoid any transient phenomena and contamination of different harmonics in the system. For these experiments a sweep rate of 0.05 Hz/s is applied, respecting the international standard ISO-7626 indications. The frequency range embraces assembly [1] first and second mode in water.

5.1. *Added mass*

Let us consider the transfer function $H_{exp}^{[1]}$ between the displacement $W_x^{[1]}$ along x of the grid with vertical position Z_w, and the force F_g applied by the actuator on grid with

position Z_f. Since the data are acquired with a swept sinusoidal excitation, the transfer functions are calculated using the cross-correlation product, and are defined as

$$H_{exp}^{[1]} = \left\| \frac{W_x^{[1]} \star W_x^{[1]}}{W_x^{[1]} \star F_x} \right\|, \tag{5.1}$$

where $W_x^{[1]} \star W_x^{1]}$ is the spectral autocorrelation of the displacement signal of the 1^{st} assembly along the x direction and $W_x^{[1]} \star F_x$ is the spectral cross-correlation between the displacement signal of the 1^{st} assembly and the force imposed on the first assembly. Cross correlation functions are calculated using an Hamming windowing filter (5000 points per windows) to clean up the noise from the signal.

The theoretical transfer function modulus for a one degree of freedom system is given by

$$H_{theo}^{[1]}(\Omega) = \frac{1}{\sqrt{(K_e - \Omega^2 M_e)^2 + \Omega^2 C_e^2}}, \tag{5.2}$$

where M_e, C_e and K_e are the coefficients of mass, damping and stiffness identified and Ω is the circular frequency.

Assembly [1] is excited around its first mode; to identify its dynamical properties, one has to find M_e, C_e and K_e that make $H_{theo}^{[1]}$ fit the experimental data $H_{exp}^{[1]}$. This can be easily achieved by a conjugate gradient optimization method.

Using an Euler-Bernoulli beam model for the rods as described in Eq. (2.1), one can write the virtual work of assembly [1]

$$\begin{aligned} M_t \int_0^L \partial_T^2 W_x^{[1]} \delta W \, dZ + C_t \int_0^L \partial_T W_x^{[1]} \delta W \, dZ + B_t \int_0^L \partial_Z^2 W_x^{[1]} \partial_Z^2 \delta W \, dZ \\ = \int_0^L F_g \delta_{Z_f} \delta W \, dZ, \end{aligned} \tag{5.3}$$

with

$$M_t = M_s + M_f, \quad B_t = B + B_f, \tag{5.4}$$

where M_f and B_f are respectively the participation of the fluid into mass and stiffness, C_t is a linear damping coefficient and the sum accounts for the 64 rods inside the assembly.

When the structure vibrates on its j^{th} natural mode

$$W_x^{[1]}(Z,T) = N_j(T) X_j(Z), \tag{5.5}$$

with $X_j(Z) = \chi_j(Z/A)$, one can rewrite the energy of the system

$$M_t \int_0^L X_j^2 dZ \, \partial_T^2 N_j + C_t \int_0^L X_j^2 dZ \, \partial_T N_j + B_t \int_0^L (\partial_Z^2 X_j)^2 dZ \, N_j = F_g X_j(Z_f). \tag{5.6}$$

Noting that the experimental signal is

$$W_g^{[1]} = N_1(T) X_1(Z_w), \tag{5.7}$$

one can relate the mass per unit of length to the identified coefficient

$$M_t = \frac{X_1(Z_f) X_1(Z_w)}{\int_0^L X_1^2 dZ} M_e. \tag{5.8}$$

Measurements take into account the effect of the fluid added mass M_f and the mass

Table 2: Values of added mass $M_x^{[1]}$

$M_x^{[1]}$	EXPERIMENT	SIMULATION
Large confinement	4.06 kg/m	7.09 kg/m
Narrow confinement	10.36 kg/m	7.78 kg/m

of the structure M_s, therefore to isolate the fluid added mass the participation of the structure is subtracted based on experimental results obtained in air. Finally, one then obtains the results listed in Table 2 where added mass are provided for the whole assembly

$$M_x^{[1]} = M_f. \tag{5.9}$$

To get a comparison with results from numerical simulation obtained in §4, the following transformation is applied

$$M_x^{[1]} = \rho A^2 \, m_x^{[1]}, \tag{5.10}$$

with $\rho = 1000\,\mathrm{kg\,m^{-3}}$ the water density.

Table 2 shows the values of added mass for large and narrow confinement given by experiments and simulations. Both agree on the increase of added mass when the confinement gets narrower. Experiments give a large increase, more than double, whereas simulations predict an increase of about 10%. Although the order of magnitude is respected the differences observed could cast doubt on the validity of the model. To properly analyse these results, one has to keep in mind that the methodology used to obtain the experimental results is subject to uncertainties coming from the accuracy of measurement, the optimization process and the fact that we try to identify constants of a linear one degree-of-freedom system from a complex nonlinear system. As a result one could estimate that the added mass coefficient given by the simulations is a reasonable estimation.

The added stiffness is orders of magnitude smaller than the "in air" structural stiffness: the added stiffness estimated from simulations in §4 is about $4.7\,\mathrm{N\,m^2}$, while the measured flexural stiffness of a fuel assembly is about $2300\,\mathrm{N\,m^2}$. As a consequence, we cannot extract the added stiffness from the total stiffness measured experimentally.

5.2. *Coupling*

To characterise the coupling between the fuel assemblies induced by the fluid, let us consider the transfer function between the imposed displacement and the displacement of the other fuel assemblies at the third grid level in the two transverse directions. Similarly to (5.1) transfer functions are calculated as

$$H_\circ^{[n]} = \left\| \frac{W_\circ^{[n]} \star W_\circ^{[n]}}{W_\circ^{[n]} \star W_x^{[1]}} \right\|, \ \circ \in \{x, y\}, \tag{5.11}$$

with $W^{[n]}$ being the displacement signal of the n-th assembly along the $\circ$ direction.

For each transfer function the maximum value, which occurs at the first natural frequency is accounted for. These experimental results are compared to displacement

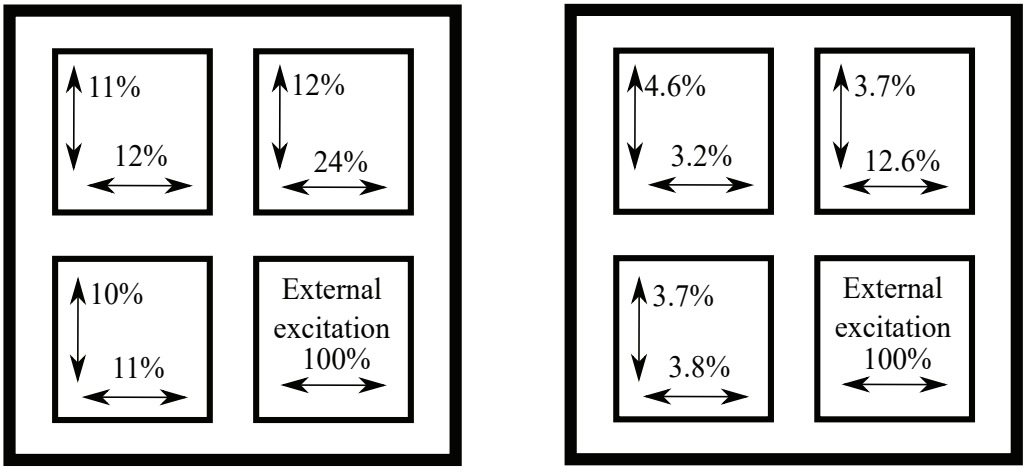

Figure 12: Displacement ratios obtained by experimental data (left) and approximated from numerical simulations (right) for 4 fuel assemblies in large confinement at first natural frequency.

ratio given by (4.10), with the addedd mass coefficients $m_\circ^{[n]}$ given in table 1 and c_v and ω_{res} estimated from identification of dynamical parameters using (5.6) as follows

$$C_v = \frac{X_1(Z_f)X_1(Z_w)}{\int_0^L X_1^2 dZ} C_e, \quad c_v = \frac{C_v}{\rho U A}, \quad \omega_{\text{res}} = \frac{A}{U}\sqrt{\frac{K_e}{M_e}}. \tag{5.12}$$

Experimental values give $c_v = 69.2$ and $\omega_{\text{res}} = 0.12$.

Figure 12 compares graphically the displacement ratios as observed in the experiments with the ratios predicted by (4.10) with these values of c_v and ω_{res}. Experiments show a ratio of about 10 % for most of the fuel assemblies in the two directions except for fuel assembly [3] which shows a coupling of about 20 % in the direction of forcing. Although simulations seem to underestimate the values of coupling, they give a good prediction of the order of magnitude. Moreover, the general pattern is well reproduced with a significantly more important coupling for fuel assembly [3] in the direction of forcing. Therefore, the methodology developed seems to be appropriate to simulate the coupling between fuel assemblies.

6. Conclusions

In this paper a new model for fluid-structure interaction of PWR fuel assemblies is proposed. The model used the well known potential flow theory and the equations are solved by using a Fourier approach. This approach leads to the important result of relating the fluid-structure interaction forces directly to the displacement of the structure itself. This result is an important achievement since it allows to drastically reduce computational time, avoiding the necessity of solving fluid equations. As a drawback it should be considered that the assumption of potential flow leads to completely neglect the fuel grids, which introduce vorticity in the flow.

Calculations with a potential flow model are first performed for a single cylinder geometry and results have been compared with reference works in literature. The model showed perfect agreement with the Slender Body Model and it also shows good predictions with respect to the confinement size. The model has been validated, and thus the mathematical

approach used to solve the equations has been demonstrated to be consistent and reliable. The model was thus improved for multiple-cylinder geometries.

Finally, in order to validate the multiple cylinders model, calculations simulating the ICARE geometry are discussed and compared with experimental results. Modal parameters are identified as functions of the flow rates and compared with experimental ones. The model reasonably fits experimental data for the added mass and gives a good estimation of the coupling between fuel assemblies.

Many perspectives are opened as a result of this work. As discussed in this paper, the model which has been implemented does not account for viscous forces. An improvement that would be of fundamental importance is to introduce with empirical factors the viscous forces in the model. One possible way to do this is to introduce viscosity in the model is to consider the axial water flow as the sum of two flows: a potential bulk flow and a viscous flow which has a defined empirical distribution. In this way the viscous forces would be taken into account with an empirical formulation, and it would be extremely interesting to assess the effects of such improvements, especially on the added damping coefficient estimation.

Acknowledgement

The authors are grateful for the financial support of the Electricité de France (EDF) and FRAMATOME.

Declaration of Interests

The authors report no conflict of interest.

REFERENCES

Bauchau, O. A. & Craig, J. I. 2009 *Structural Analysis: With Applications to Aerospace Structures*. Springer.

Blevins, R.D. 2015 *Formulas for Dynamics, Acoustics and Vibration*. John Wiley & Sons, Ltd.

Brennen, C.E. 1982 A review of added mass and fluid inertial forces. *Technical Report Naval Civil Engineering Laboratory, Sierra Madre, CA, USA* .

Buat, D. 1779 *Principles d'hydraulique*. Monsieur le Chevalier Du Buat.

Capanna, R. 2018 Modelling of fluid structure interaction by potential flow theory in a PWR under seismic excitation. PhD thesis, Ecole Centrale Marseille, France.

Capanna, R., Ricciardi, G., Eloy, C. & Sarrouy, E. 2019 Experimental study of fluid structure interaction on fuel assemblies on the icare experimental facility. *Nuclear Engineering and Design* **352**, 110146.

Chen, S.S. 1985 Flow-induced vibration of circular cylindrical structures. *Tech. Rep.*. Argonne National Lab.(ANL), Argonne, IL (United States).

Chen, S.S. & Wambsganss, M.W. 1972 Parallel-flow-induced vibration of fuel rods. *Nuclear Engineering and Design* **18** (2), 253–278.

Classen, P. 1972 Die 'hydrodynamische masse' eines rohrs in einem rohrbundel. *Forschung im Ingenieurwesen A* **38** (2), 33–37.

De Langre, E., Païdoussis, M.P., Doaré, O. & Modarres Sadeghi, Y. 2007 Flutter of long flexible cylinders in axial flow. *Journal of Fluid Mechanics* **571**, 371–389.

De Mario, E. & Street, B.D. 1989 Nuclear fuel rod grid spring and dimple structures. US Patent 4,803,043.

De Ridder, J., Degroote, J., Van Tichelen, K. & Vierendeels, J. 2013 Modal characteristics of a flexible cylinder in turbulent axial flow from numerical simulations. *Journal of Fluids and Structures* **43**, 110–123.

De Ridder, J., Degroote, J., Van Tichelen, K. & Vierendeels, J. 2017 Predicting modal characteristics of a cluster of cylinders in axial flow: from potential flow solutions to coupled CFD-CSM calculations. *Journal of Fluids and Structures* **74**, 90–110.

De Ridder, J., Doaré, O., Degroote, J., Van Tichelen, K., Schuurmans, J. & Vierendeels, J. 2015 Simulating the fluid forces and fluid-elastic instabilities of a clamped-clamped cylinder in a turbulent flow. *Journal of Fluids and Structures* **55**, 139–154.

Doaré, O., Mano, D. & Bilbao Ludena, J. C. 2011*a* Effect of spanwise confinement on flag flutter: experimental measurements. *Physics of Fluids, American Institute of Physics* **23**, 11704.

Doaré, O., Sauzade, M. & Eloy, C. 2011*b* Flutter of an elastic plate in a channel flow: confinement and finite-size effects. *Journal of Fluids and Structures* **27** (1), 76–88.

Eloy, C., Doaré, O., Duchemin, L. & L., Schouveiler 2010 A unified introduction to fluid mechanics of flying and swimming at high reynolds number. *Experimental Mechanics* **50** (9), 1361–1366.

Eloy, C., Lagrange, R., Souilliez, C. & Schouveiler, L. 2008 Aeroelastic instability of cantilevered flexible plates in uniform flow. *Journal of Fluid Mechanics* **611**, 97–106.

Eloy, C., Souillez, C. & Schouveiler, L. 2007 Flutter of a rectangulare plate. *Journal of Fluids and Structures* **23** (6), 904–919.

Gosselin, F.P. & De Langre, E. 2011 Drag reduction by reconfiguration of a poroeslatic system. *Journal of Fluids and Structures* **27** (7), 1111–1123.

Guo, C.Q. & Païdoussis, M. P. 2000 Stability of rectangular plates with free side-edges in two-dimensional inviscid channel flow. *Journal of Applied Mechanics* **67** (1), 171–176.

Hecht, F. 2012*a* Freefem++ v.3.19-1. *Université Pierre et Marie Curie. http://www.freefem.org/ff++/ftp/freefem++doc.pdf* .

Hecht, F. 2012*b* New development in FreeFem++. *Journal of Numerical Mathematics* **20** (3-4), 251–265.

Lamb, H. 1895 Hydrodynamics. *Cambridge University Press* .

Lighthill, M.J. 1960*a* Mathematics and Aeronautics. *The Journal of the Royal Aeronautical Society* **64** (595), 375–394.

Lighthill, M.J. 1960*b* Note on the swimming of slender fish. *Journal of Fluid Mechanics* **9** (2), 305–317.

Michelin, S. & Smith, S.L. 2009 Linear stability analysis of coupled parallel flexible plates in an axial flow. *Journal of Fluids and Structures* **25** (7), 1136–1157.

Morison, J.R., Johnson, J.W. & Schaaf, S.A. 1950 The force distribution exerted by surface waves on piles. *Journal of Petroleum Technology* **2** (5), 149–154.

Païdoussis, M. P. 1966*a* Dynamics of slender cylinders in axial flow: Part 1 Theory. *Journal of Fluid Mechanics* **26** (4), 717–736.

Païdoussis, M. P. 1966*b* Dynamics of slender cylinders in axial flow: Part 2 Experiments. *Journal of Fluid Mechanics* **26** (4), 737–751.

Païdoussis, M. P. 1973 Dynamics of cylindrical structures subjected to axial flow. *Journal of Sound and Vibration* **29** (3), 365–385.

Païdoussis, M. P. 1979 The dynamics of clusters of flexible cylinders in axial flow: theory and experiments. *Journal of Sound and Vibration* **65** (3), 391–417.

Païdoussis, M. P. & Pettigrew, M.J. 1979 Dynamics of flexible cylinders in axisymetrically confined axial flow. *Journal of Applied Mechanics* **46** (1), 37–44.

Païdoussis, M. P. & Suss, S. 1977 Stability of a cluster of flexible cylinders in bounded axial flow. *Journal of Applied Mechanics* **44** (3), 401–408.

Païdoussis, M. P., Suss, S. & Pustejovsky, M. 1977 Free vibration of clusters of cylinders in liquid-filled channels. *Journal of Sound and Vibration* **55** (3), 443–459.

Pettigrew, M.J. & Taylor, C.E. 2003 Vibration analysis of shell-and-tube heat exchangers: an overview—part 1: flow, damping, fluidelastic instability. *Journal of fluids and structures* **18** (5), 469–483.

Ricciardi, G., Bellizzi, S., Collard, B. & B., Cochelin 2009 Modelling Pressurized Water Reactor cores in terms of porous media. *Journal of Fluids and Structures* **25** (1), 112–133.

Schouveiler, L. & Eloy, C. 2009 Coupled flutter of parallel plates. *Physics of Fluids* **21** (8).

Singh, K., Michelin, S. & De Langre, E. 2012 Energy harvesting from fluid-elastic instabilities of a cylinder. *Journal of Fluids and Structures* **30**, 159–172.

Taylor, G.I. 1952 Analysis of the swimming of long and narrow animals. *Proceedings of the Royal Society* **214** (1117), 158–183.

Triantafyllou, G.I. & Cheryssostomidis, C. 1985 Stability of a string in axial flow. *ASME Journal of Energy Ressources Technology* **107** (421), 421–425.

Wendel, K. 1956 Hydrodynamic masses and hydrodynamic moments of inertia. *TMB Translation* **260**.

Wu, T.Y. 2001 Mathematical biofluiddynamics and mechanophysiology of fish locomotion. *Mathematical Methods in the Applied Sciences* **24** (17-18), 1464–1541.

Appendix A. FreeFEM++ code for one cylinder

```
real k = 0.01;
real lx = 1.5;
real ly = 2;
real A = 1.;

// Geometry
border Cxb(t=0, 1){x=A+(lx-A)*t^(2); y=0*t; label=1;}
border Cyr(t=0, 1){x=lx+0*t; y=tan(atan(ly/lx)*t)/tan(atan(ly/lx))*ly; label=2;}
border Cxt(t=0, 1){x=tan(atan(lx/ly)*(1-t))/tan(atan(lx/ly))*lx; y=ly+0*t; label=2;}
border Cyl(t=0, 1){x=0*t; y=A+(ly-A)*(1-t)^(2); label=2;}
border Beam(t=0, pi/2){x=A*cos(t); y=A*sin(t); label=3;}

// Mesh
real ds = 1/k/10;
int NbA = max(ceil(pi/2*A/ds),21.);
int Nbx = ceil(atan(lx/ly)/(pi/2)*(NbA))+1;
int Nby = ceil(atan(ly/lx)/(pi/2)*NbA)+1;
int NbxmA = ceil((lx-A)/lx*NbA)+1;
int NbymA = ceil((ly-A)/ly*NbA)+1;
mesh cMesh = buildmesh(Cxb(NbxmA) + Cyr(Nby) + Cxt(Nbx) + Cyl(NbymA) + Beam(-NbA));

// FE
fespace Vh(cMesh,P2);
Vh u, v;

// Resolution
solve pFourier(u,v)
  = - int2d(cMesh)(u*v*k^2 + dx(u)*dx(v) + dy(u)*dy(v))
    + int1d(cMesh,3)(y/A*v)
    + on(1,u=0);

// mu computation
real mu = 0;
mu = -4*int1d(cMesh,3)(-u*y/A);
```

Appendix B. Qualitative analysis

After solving numerically the Helmholtz problem (4.1) for $\hat{\gamma}_x^{[1]} = 1$, the resulting forces on each rod q of each assembly n can be evaluated in both the x and y directions. From this, we can calculate the associated added masses $\hat{\mu}_x^{[n,q]}$ and $\hat{\mu}_y^{[n,q]}$

$$\hat{\mu}_x^{[n,q]} = \int_{\partial\mathcal{C}^{[n,q]}} \hat{p}\cos(\theta)\, d\theta, \tag{B 1a}$$

$$\hat{\mu}_y^{[n,q]} = \int_{\partial\mathcal{C}^{[n,q]}} \hat{p}\sin(\theta)\, d\theta, \tag{B 1b}$$

with $\partial\mathcal{C}^{[n,q]}$ the boundary of the rod q in assembly n. Note that $\hat{\mu}_x^{[n,q]}$ and $\hat{\mu}_y^{[n,q]}$ are unchanged when k is changed into $-k$ since k always appears squared in the problem.

These added masses are illustrated in Figures 13 and 14 for the 8 mm confinement.

Analogy with the one cylinder case explains the positive values observed on assembly [1] for

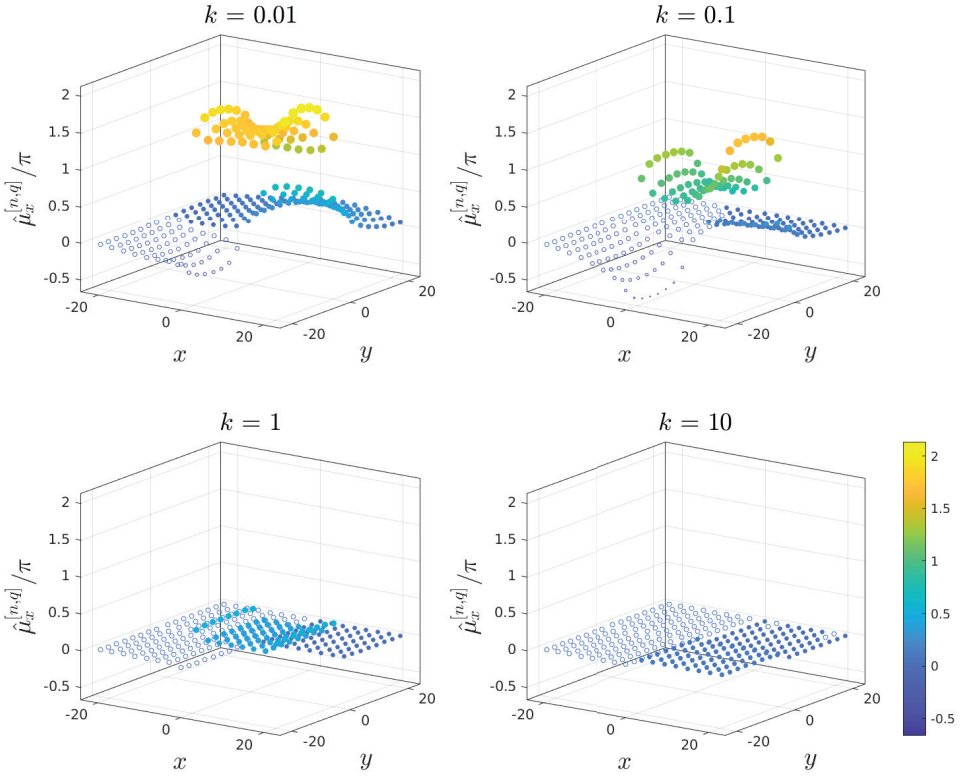

Figure 13: Added mass along x $\hat{\mu}_x^{[n,q]}$ for each rod for four values of k as labelled. Full circles note positive values, hollow ones negative values. The confinement is 8 mm.

$\hat{\mu}_x^{[n,q]}$. Confinement size is about the rod diameter, that may be compared to $l_x = l_y = 3$ in the previous section for which $\hat{\mu} > \pi$ when $k \ll 1$. This is consistent with the values observed for assembly [1] (even though the rods are not properly confined). An interesting result is that rods in assemblies [2] to [4] experience very small forces. As noted in §3.5, this phenomenon is all the more true as k becomes large: pressure perturbations remain closer to the moving rods when k is large and interactions with far away rods are almost negligible.

Appendix C. Calculation of pressure forces in physical space

In §4.3, we explained how to compute numerically the functions $\hat{\mu}_\circ^{[n]}(k)$, which are then interpolated with piecewise 6th-order polynomials. These interpolations can be used to compute the added masses $\mu_\circ^{[n]}(z)$ with an inverse Fourier transform (Figure 15).

The functions $\mu_\circ^{[n]}(z)$ are needed in (4.4*a–c*) to compute the added mass, added damping, and added stiffness matrices. Note that the functions $\mu_\circ^{[n]}(z)$ are non-zero on an interval $\Delta z \lesssim 100$ (figure 15). This means that on a z-scale of order $l = L/A \approx 571$, these functions are almost proportional to a Dirac function, such that the convolution products between $\mu_\circ^{[n]}$ and χ_j, χ_j', or χ_j'' appearing in (4.4*a–c*) can be approximated by simple product with $\int_{-\infty}^{\infty} \mu_\circ^{[n]}\, dz$.

As a consequence, the added mass matrix $\boldsymbol{M}_\circ^{[n]}$ and the added stiffness matrix $\boldsymbol{K}_\circ^{[n]}$ are almost diagonal (since $\langle \chi_i, \chi_j \rangle = \delta_{ij}$) and the diagonal terms of the added damping matrix $\boldsymbol{C}_\circ^{[n]}$ are almost zero (since $\langle \chi_i, \chi_i' \rangle = 0$). This can be verified by computing the first 3×3 terms of the matrices $\boldsymbol{M}_x^{[n]}$ and $\boldsymbol{C}_x^{[n]}$ for $n = 1$ and 4 (we chose assembly [4] because it is the assembly for

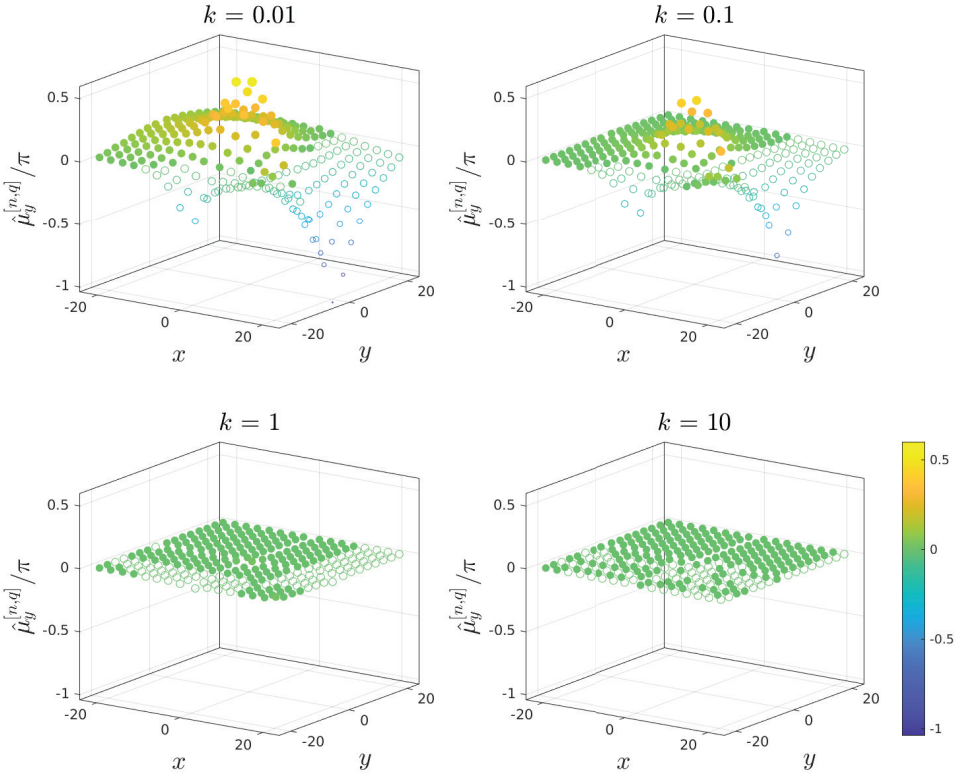

Figure 14: Same as Figure 13 for the y-component of the added mass: $\hat{\mu}_y^{[n,q]}$.

which the extension of $\mu_x^{[n]}(z)$ is widest, see figure 15)

$$\boldsymbol{M}_x^{[1]} = \begin{pmatrix} 350 & 0 & 0.0182 \\ 0 & 347 & 0 \\ 0.0182 & 0 & 342 \end{pmatrix}, \tag{C 1a}$$

$$\boldsymbol{M}_x^{[4]} = \begin{pmatrix} 18.6 & 0 & 0.0882 \\ 0 & 17.4 & 0 \\ 0.0882 & 0 & 15.4 \end{pmatrix}, \tag{C 1b}$$

$$\boldsymbol{C}_x^{[1]} = \begin{pmatrix} 0 & -3.26 & 0 \\ 3.26 & 0 & -5.79 \\ 0 & 5.79 & 0 \end{pmatrix}, \tag{C 1c}$$

$$\boldsymbol{C}_x^{[4]} = \begin{pmatrix} 0 & -0.167 & 0 \\ 0.167 & 0 & -0.272 \\ 0 & 0.272 & 0 \end{pmatrix}. \tag{C 1d}$$

Note that the matrices $\boldsymbol{K}_\circ^{[n]}$ satisfy $(\boldsymbol{K}_\circ^{[n]})_{ij} = -k_j^2(\boldsymbol{M}_\circ^{[n]})_{ij}$, such that they share the same characteristic of being almost diagonal with the matrices $\boldsymbol{M}_\circ^{[n]}$.

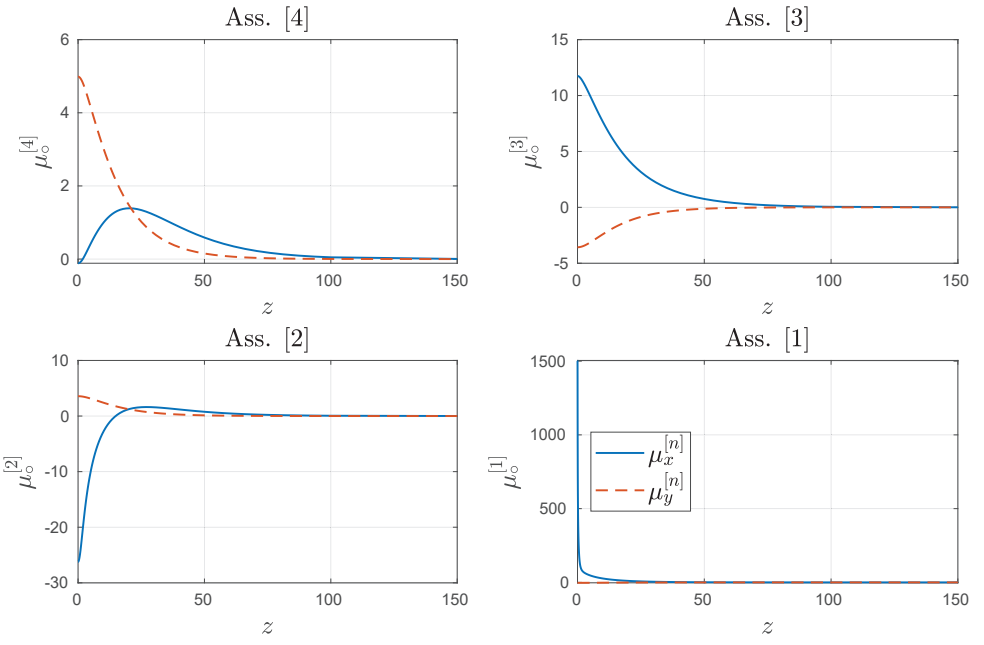

Figure 15: Added mass $\mu_x^{[n]}(z)$ (blue solid line) and $\mu_y^{[n]}(z)$ (red dashed line) as a function of z for the different assemblies (large confinement).